ACS APPLIED MATERIALS & INTERFACES

Research Article

www.acsami.org

Ruthenium Polypyridyl TG6 Dye for the Sensitization of Nanoparticle and Nanocrystallite Spherical Aggregate Photoelectrodes

M. Hosni,[†,‡] Y. Kusumawati,[†,§] S. Farhat,[‡] N. Jouini,[‡] A. L. Ivansyah,[§] M. A. Martoprawiro,[§] and Th. Pauporté*[,†]

[†]Institut de Recherche de Chimie-Paris, CNRS − Chimie ParisTech − PSL, UMR8247, 11 rue Pierre et Marie Curie, 75005 Paris, France

[‡]Laboratoire des Sciences des Procédés et des Matériaux, LSPM UPR 3407, Université Paris 13/CNRS, Sorbonne Paris Cite, 93430 Villetaneuse, France

[§]Inorganic and Physical Chemistry Division, Faculty of Mathematics and Natural Sciences, Institut Teknologi Bandung (ITB), Jl. Ganesha 10, Bandung 40132, Indonesia

Supporting Information

ABSTRACT: A ruthenium polypyridyl dye containing a hexasulfanyl-styryl modified bipyridyl group as ancillary ligand, coded TG6, is investigated as a sensitizer for ZnO-based dye-sensitized solar cells (DSSCs). The advantages of this dye are a broad wavelength absorption spectrum, a large loading in ZnO photoelectrodes, a significantly larger extinction coefficient compared to more classical Ru-polypyridyl dyes, and the formation of less agglomerate in the pores of the ZnO layers. TG6 has been used to sensitize ZnO nanorod particle layers of high structural quality and ZnO layers made of submicrometer spheres composed of aggregated nanocrystallites and that develop an internal surface area. The latter are highly light-scattering in the visible wavelength region but more difficult to sensitize correctly. The TG6 dye has been compared with the metal-free D149 dye and has been shown more efficient for photoconversion. The best performances have been obtained by combining TG6 with the nanorod layer, the optimal power conversion efficiency being measured at 5.30% in that case. The cells have been investigated by impedance spectroscopy over a large applied voltage range. We especially show that the submicrometer sphere layers exhibit lower conductivity and lower charge collection efficiency as compared to the nanorod particle ones.

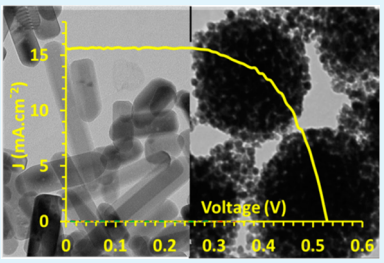

KEYWORDS: *TG6, ZnO, polyol process, dye-sensitized solar cells, impedance spectroscopy*

INTRODUCTION

During the past two decades, dye-sensitized solar cells (DSSCs) have attracted increasing attention. DSSCs are low cost, easy to handle, and have a relatively high conversion efficiency.[1−4] A typical DSSC consists of a mesoporous TiO_2 film sensitized by a monolayer of dye molecules, impregnated by an electrolyte containing a redox shuttle and completed by a counter electrode.[2] The use of ZnO as an alternative to TiO_2 as a wide bandgap electron transport material has received much less attention. ZnO is an interesting material for application in DSSC since it shows fast charge transport with electron mobility and conductivity several orders of magnitude higher compared to anatase TiO_2.[5,6] Fast transport will increase the charge collection efficiency and facilitate the change of redox shuttle in the solar cells notably to get higher open circuit voltage (V_{oc}).[4,7] ZnO can be easily grown as nanostructured films and various nanostructures have been described in the literature.[8−15] In addition, the synthesis of highly crystalline ZnO layers at low temperature has been performed by several techniques compatible with substrates that do not tolerate heat treatments.

In the case of TiO_2, mesoporous films are usually prepared by sintering colloidal particles as reported in the pioneering DSSC paper by Grätzel and O'Regan[1] and is the most successful process in terms of final energy conversion performance up to now.[4] In the case of ZnO, the forced hydrolysis in polyol medium technique is a very interesting synthetic route for the preparation of both nanoparticles and nanoparticle superstructures.[16−23] This technique is cost-effective, easy to implement, and simple to scale up with reproducible results. It has been used for the synthesis of various inorganic compounds[16,17] and pure metals[18−20] at rather low temperatures. The interesting properties of diol media include their high dielectric constants (between 20 and 40) and their solvation properties for many inorganic precursors.[21] Moreover, they offer a wide operating-temperature range for the preparation of inorganic compounds because they have a relatively high boiling point. The polyol molecules act as a solvent in the synthesis, as a complexing agent, and as a surfactant agent which adsorbs on the surface of the elementary particles preventing or controlling their aggregation.[23] The technique can produce nanoparticle super-

Received: October 6, 2014
Accepted: December 29, 2014
Published: December 29, 2014

DOI: 10.1021/am5068645
ACS Appl. Mater. Interfaces 2015, 7, 1568−1577

Scheme 1. Molecular Structures of TG6 and D149 Dyes

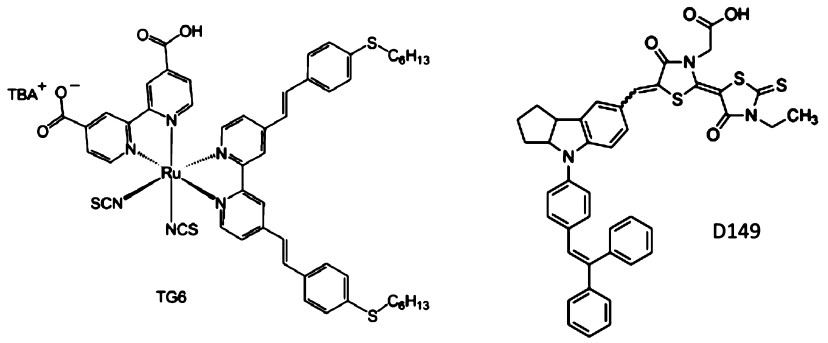

structures such as spherical aggregates with controlled submicrometer size.[9−11,24,25] These structures are attractive for DSSC application since they are highly visible light scattering, and they consequently present light trapping properties.[10]

Finding appropriate dyes to raise the ZnO−DSSC performance at the level of the TiO_2 based-ones remains challenging. Indeed, the ZnO solar cell efficiency is clearly limited by a less attached dye density and by more recombination side reactions.[6,26] In the literature, the best ZnO-based DSSC performances have been achieved using the N3 or N719 ruthenium-based dyes (the molecular structures of the cited dyes are presented in Scheme S1, Supporting Information) since some authors have reported overall conversion efficiencies ranging 6.5−7.5% for these systems.[27−29] The best short circuit current, J_{sc}, has been measured above 19 mA.cm^{-2}, which is close to the J_{sc} of the best TiO_2-based DSSCs.[4] However, all our attempts to reproduce these data have proved to be unsuccessful.[26] The low conversion efficiency of most ZnO-based DSSC prepared using N719 is likely due to the dissolution of the ZnO and Zn(II) generation by the adsorbed acidic dye, which is followed by the formation of agglomerates. The agglomerates produce an insulating layer of Zn^{2+} and ruthenium photosensitizer molecules at the oxide surface, and, eventually, can block the injection of electrons from the dye molecules to the semiconductor by the insulating layer.[30−32] On the other hand, some efficient organic sensitizers, such as indoline derived molecules, have been developed during the last years for the sensitization of ZnO. Their molar extinction coefficients are significantly higher than those of the common ruthenium photosensitizers.[33,34] The D149 indoline dye has a rhodanine dimer as the acceptor group and a carboxylic acid as the anchoring group (Scheme 1). D205 is an amphiphilic derivative of D149 in which the ethyl chain bound to a N of rhodanine is replaced by an octyl chain that is supposed to limit the dye aggregation upon the sensitization step. Using the D149 dye, we have reported a power conversion efficiency (PCE) of 4.64% with electrodeposited mesoporous ZnO films[35] and 4.66% with nanoparticle films.[23] Cheng and Hsieh obtained a PCE of 4.95% and 5.34% for self-asssembled ZnO secondary nanoparticles photoelectrodes sensitized with D149 and D205 dyes, respectively.[10] Magne et al. have recently shown that the D149 dye could be co-sensitized with the complementary D131 dye in order to get an incident photon-to-electron conversion efficiency (IPCE) of about 80% between 400 and 600 nm. This enhanced the PCE by 8% compared to the use of the D149 dye alone.[36] Higashijima et al. have reported that two novel indoline dyes, coded DN319 and DN350, developed for ZnO-based DSSCs, could raise the PCE up to 5.01%[37] and 5.55%,[38] respectively.

In the present work, we introduce the use of a ruthenium polypyridyl dye containing a hexasulfanyl-styryl modified bipyridyl group as ancillary ligand, coded TG6 (Scheme 1), for ZnO photoelectrode sensitization. This dye has been very poorly documented in the DSSC literature in spite of reported performances close to that of the reference N719 dye in the case of TiO_2 sensitization.[39,40] We show that TG6 is highly relevant combined with porous photoelectrodes made of ZnO rod-like nanoparticles and ZnO nanocrystallite spherical aggregates. Due to the two long alkyl chains in its molecular structure, the ZnO degradation and the agglomeration are markedly reduced. We compare TG6 performance with the D149 reference indoline dye. To better understand the effect of dye and nanostructure on the cell functioning, a detailed study by impedance spectroscopy (IS) has been carried out.

2. EXPERIMENTAL SECTION

2.1. ZnO Structure and Layer Preparations. Controlled ZnO nanostructure have been prepared by the polyol process with adjusted parameters. A controlled amount of zinc acetate dihydrate ($Zn(OAc)_2.2H_2O$), and an appropriate volume of distilled water were successively added to diethylene glycol (DEG, with formulas $O(CH_2CH_2OH)_2$). The size and morphology of the ZnO particles were controlled by adjusting the growth temperature, the zinc concentration (z), and the hydrolysis ratio defined as $h = (n_{H_2O})/(n_{Zn^{2+}})$ where n_{H_2O} and $n_{Zn^{2+}}$ account for the molar number of water and zinc precursor, respectively.[23] The mixture was then heated under reflux for 1 h. The obtained white precipitate of zinc oxide nanocrystallites (NR35) or aggregates (AG200) was centrifuged, washed several times successively with ethanol and acetone, and dried at 60 °C. The NR35 rod-shaped particles were prepared in DEG at 161 °C with z = 0.5 mol·L^{-1} and h = 5. The ZnO nanocrystallite hierarchical aggregates (AG200) were prepared in DEG at 130 °C with z = 0.09 mol·L^{-1} and h = 2.

The layers were prepared as described elsewhere.[23] A paste was created by mixing 1.5 g of NR35 ZnO nanoparticles powder or 1 g of AG200 ZnO aggregate powder with 5 g of ethanol, 0.28 g of ethyl cellulose (5−15), 0.11 g of ethyl cellulose (30−70), and 4 g of terpineol. These compositions gave rise to a porosity, p, of about 60% for all the investigated films. Fluorine-doped SnO_2 (FTO) coated glass sheets (TEC-15 from Solaronix) substrates were carefully cleaned with detergent, deionized water, acetone, and finally ethanol in an ultrasonic bath for 5 min each. A film was deposited by doctor-blading the paste on top of the FTO substrate.[6] The nanoparticle layer was annealed at 410 °C for 30 min as described elsewhere.[34] In the case of the AG200 ZnO nanocrystallite aggregate, we have investigated the effect of the sintering layer temperature on the cell performances. As shown in the Supporting Information (Table S1 and Figure S1), the best efficiency was achieved using 400 °C as the annealing temperature.

DOI: 10.1021/am5068645
ACS Appl. Mater. Interfaces 2015, 7, 1568−1577

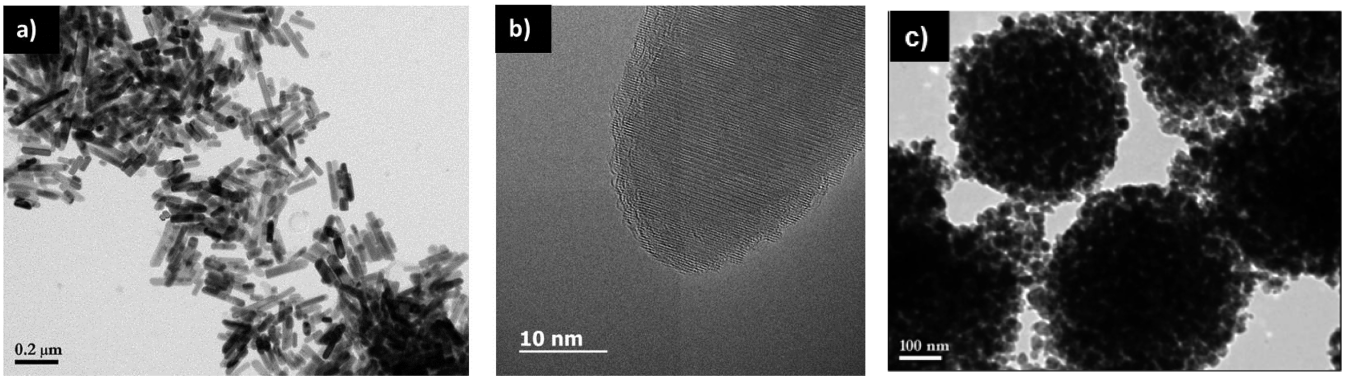

Figure 1. (a) TEM image of NR35 nanorods. (b) High resolution TEM image of an individual NR35 nanorod. (c) TEM image of AG200 nanocrystallite aggregates.

The layer thickness was measured with a Dektak 6 M stylus profiler. This parameter was optimized for the two kinds of particles to get the best efficiency. The effect of this parameter on the AG200 cell performance is presented in the Supporting Information (Table S2 and Figure S2). The best performances were achieved for layers with a thickness ranging between 27 and 32 μm. The XRD patterns were determined by a Phillips X'pert high-resolution X-ray diffractometer operated at 40 kV and 45 mA using Cu Kα radiation with λ = 1.5406 Å and a rotating sample holder was used. The size and the shape of the ZnO particles/aggregates were determined using a JEOL 2011 transmission electron microscope (TEM) operated at 200 kV. The sample morphologies were examined with a high resolution Ultra 55 Zeiss FEG scanning electron microscope (FE-SEM) at an acceleration voltage of 10 kV.

2.2. Solar Cell Preparation and Characterizations. The layers were sensitized with the TG6 dye (cis-bis(thiocyanato)(2,20-bipyridyl-4,40-dicarboxylato){4,40-bis[2-(4-hexylsulfanylphenyl)vinyl]-2,20-bipyridine}ruthenium(II) mono(tetrabutylammonium) salt) (Borun chemicals) which molecular structure is presented in Scheme 1. The ZnO layers were immersed, after 5 min of cooling, in a 0.3 mM TG6 in dichloromethane CH_2Cl_2 solution. For the sake of comparison, cells prepared with the D149 indoline dye (Chemicrea Inc.) (5-[[4-[4-(2,2-diphenylethenyl)phenyl]-1,2,3-3*a*,4,8*b*-hexahydrocyclopent[*b*]indol-7-yl]methylene]-2-(3-ethyl-4-oxo-2-thioxo-5-thiazolidinylidene)-4-oxo-3-thiazolidineacetic acid) (Scheme 1) were also investigated. The D149 sensitization was performed in the same manner, in a 0.5 mM dye and 1 mM octanoic acid coadsorbant dissolved in a 1:1 volume mixture of acetonitrile/*tert*-butanol.[36] For the two dyes, the sensitization time was 2 h. The counter-electrode was prepared as described elsewhere.[23]

The two electrodes were sealed with a 50 μm hot melt spacer (Surlyn, DuPont) and filled with the electrolyte through a hole drilled in the counter electrode. The hole was subsequently sealed with a Surlyn piece covered by aluminum foil. The composition of the electrolyte used in the TG6 cells was 0.6 mol·L^{-1} 1,2-dimethyl-3-propylimidazolium iodide (DMPII), 0.1 mol·L^{-1} LiI, 0.05 mol·L^{-1} I_2, 0.10 mol·L^{-1} guanidinium thiocyanate, and 0.5 mol·L^{-1} 4-*tert*-butylpyridine in a mixture of acetonitrile and valeronitrile (85/15 volume ratio). The D149 cell electrolyte was 0.05 M I_2 and 0.5 M 1-2, dimethyl,3-propylimidazolium iodide (DMPII) in acetonitrile.

The $I-V$ curves were recorded by a Keithley 2400 digital sourcemeter. The voltage sweep rate was 0.01 V.s^{-1}. The solar cells were illuminated with a solar simulator (Abet Technology Sun 2000) filtered and calibrated to mimic AM 1.5G 100 mW.cm^{-2} conditions. The impedance spectra (IS) were measured in the dark over a large potential range, by a Solartron FRA1255 frequency response analyzer coupled with a PAR273 EGG potentiostat. The AC signal was 10 mV and the frequency range was 100 kHz to 0.05 Hz. The spectra were fitted and analyzed using the Zview modeling software (Scribner). The IS results were corrected for IR-Drop as described elsewhere[6] and the corrected voltage is noted as V_{cor}. The total optical transmission and reflection spectra of the photoelectrodes were recorded with a Cary 5000 UV−vis-NIR spectrophotometer equipped with an integrating sphere. The sensitized layer absorbance curves were deduced from the transmittance and reflectance spectra.

2.3. Computational Details. The calculations were carried out using the Gaussian 09 program package[41] with B3LYP exchange-correlation functional.[42] The dye geometries were optimized using the 6-311G* basis set for C, H, O, N, and S atoms[43,44] together with the Los Alamos effective core potential LanL2DZ for Ruthenium.[45−47] Solvation effects were evaluated by the conductor-like polarizable continuum model (C-PCM),[48,49] using DMF as a solvent for D149 and CH_2Cl_2 for TG6. The single point TD-DFT calculation[50] then was carried out to the optimized structure to gain insight into the electronic properties and detailed excited states behavior that contribute to the UV−vis spectra.

3. RESULTS AND DISCUSSION

In our previous work on ZnO nanoparticles prepared by the forced hydrolysis in polyol technique, we have investigated the effect of the size and shape of these particles on the DSSC performance and photoanode functioning.[23] We have shown that the rod shaped ones, viewed in Figure 1a, yielded the best PCE. The size distribution of these particles is disclosed in Figure S3a (Supporting Information (SI)). Their mean diameter is measured at 35 nm and their mean length at 100 nm. High resolution TEM images of individual rods (Figure 1b) show the high structural quality of the bulk material with perfectly stacked (001) planes and no structural defects. Moreover, the images also show the remarkable high structural quality of the rod surface. In the present work, we introduce the hierarchical spheres made of aggregated nanocrystallites prepared by the same polyol technique but with different conditions. By lowering the zinc concentration, the shape of the nanoparticle changed from rods to an aggregated small particle arrangement as clearly observed on the TEM view of Figure 1c. The size analysis of the spheres is presented in SI Figure S3b. The submicronic spheres were polydispersed in size with a diameter ranging 100−400 nm and the presence of larger spheres of 600−800 nm. Their mean value was measured at 220 nm. The mean diameter of the nanocrystallites composing the spheres was 19 nm. It may be possible that van der Waals interaction between the surfaces of these small nanocrystallites is the driving force for self-assembly. Due to the chelating effects of diethylene glycol, primary particles grow up separately and then, owing to their high surface reactivity, assemble to form secondary ZnO structures.

The NR35 and AG200 particles have been used as building blocks to prepare porous ZnO films by following the protocol described in the Experimental Section. In the layer preparation

DOI: 10.1021/am5068645
ACS Appl. Mater. Interfaces 2015, 7, 1568−1577

procedure, the annealing step has a key role since it eliminates the organic binder to release the porosity. This step also ensures the connection and necking of the particles and/or of the spheres. Their good electrical connection is required for the efficient electron transport in the final device. The optimized annealing temperature was found to range between 400 and 410 °C, for which the ethyl cellulose is reported to be fully eliminated (SI Table S1, Figure S1, and ref 34). Figure 2a is a

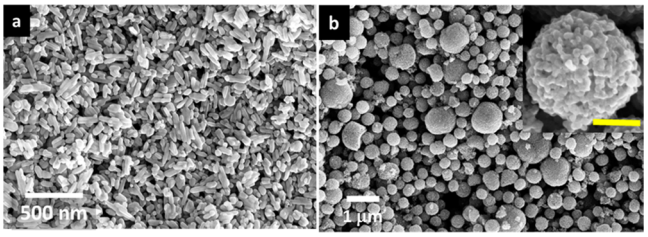

Figure 2. SEM top-view of (a) a NR35 layer and (b) a AG200 layer. The inset is a zoomed view of a sphere with a scale bar of 100 nm.

FESEM top-view of a NR35 layer. The layer is porous and some aggregations of the rods by their lateral facets are observed. Figure 2b is a FESEM top-view of the AG200 layer. It is made of the stacked sphere with a polydispersed size. The inset zoomed view of an individual sphere confirms its porous nature, and it illustrates that the pores inside the spheres are small in size.

In SI Figure S4, the XRD patterns of the films are indexed by the wurtzite hexagonal structure of ZnO with no preferential orientation. The peak enlargement in the AG200 pattern is due to the small size of the aggregated nanocrystallites composing the spheres. Using the Scherrer method described in SI Figure S4 for the (100), (002), and (101) reflections, we have determined an average crystallite size of 19 nm in good agreement with the TEM view analysis (SI below Figure S3). The films have also been characterized by photoluminescence measurements at room temperature (Figure 3A). They show a strong near-band edge emission centered around 382 nm. The high structural and surface quality of the NR35-film is attested by the strong UV emission and the very weak emission in the visible wavelength region. On the other hand, the AG200 film has a weaker emission in the UV and a marked broad emission peak in the orange-red region (centered at 604 nm). The latter can be assigned to surface defects.[6]

The reflectance spectra of the bare layers are presented in Figure 3B. The NR35 layers scatter light with a maximum of reflectance measured at 40% and centered at 398 nm. The reflectance of the aggregate layer is much stronger. Mie theory[51] and Anderson localization of light[52] provide the analytical description for the scattering of light by spherical particles and predict that resonant scattering may occur when the particle size is comparable to the wavelength of incident light. The aggregates within ZnO films are submicrometer-sized, and they are therefore particularly efficient scatterers for visible ligh due to multiple scattering of light within the hierarchical ZnO layers. We measured a maximum total reflectance, *R*%, of 72% for a wavelength of 460 nm which is red-shifted compared to the maximum of the NR35 layer. The curve of the AG200 film is better adapted to the visible light absorption by the dyes. The reflectance is remarkably high, even higher than that reported recently for films prepared from

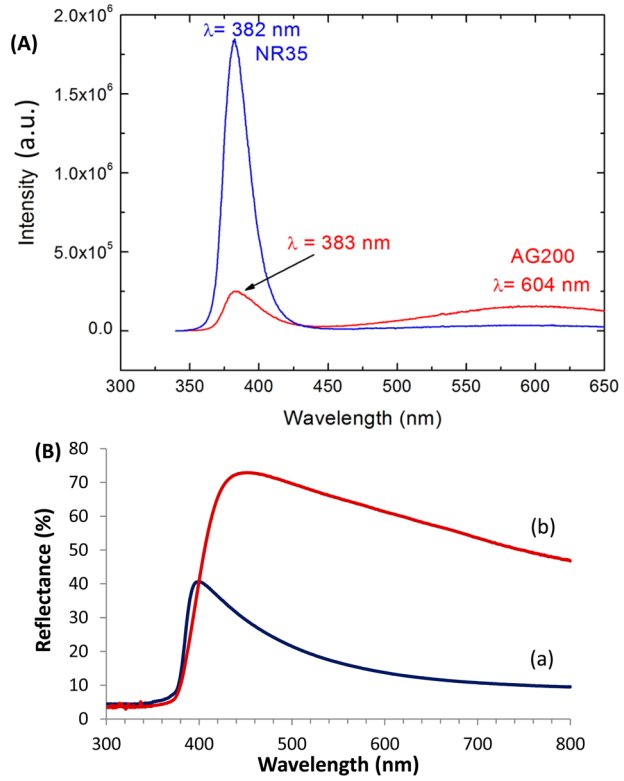

Figure 3. (A) Photoluminescence spectra measured at room temperature of naked NR35 and AG200 porous films (excitation at 266 nm). (B) Reflectance spectra of the naked films: (a) NR35 and (b) AG200 films.

a submicrometer-sized ZnO powder by the occlusion electrolysis technique.[53]

In the present study, TG6 Ru-polypyridyl has been studied as a new dye for ZnO-based DSSCs. It has been compared with the D149 organic dye. Their extinction coefficients measured in DMF are reported in Table 1. D149 has a large ε which is about 3.2 times that of TG6. However, TG6 is a ruthenium polypyridyl dye engineered in a way to have a high absorption coefficient and extended absorption in the visible region of the solar spectrum due to the extended π-conjugation of the ancillary ligand.[39] Consequently, the extinction coefficient of TG6 is higher by ~65% than that of the N719 dye (Table 1).

The UV−vis-absorption spectra of both dyes that resulted from TD-DFT calculations are presented in Figure 4 and the calculated electronic transitions with their oscillator strengths are gathered in SI Table S3. They are in agreement with the experimental measurements performed in CH_2Cl_2 and also reported in the same figure. This calculation shows that absorption at 567 nm results from the electron transition between the HOMO−2 and the LUMO orbitals. Further computational investigation found out that the HOMO−2 orbital is composed predominantly of the d orbital on ruthenium atom, which indicates that this electronic transition is a metal-to-ligand charge transfer (MLCT) transition (SI Table S3 and Figure S5b). TD-DFT calculation of D149 dye exhibits a 30 nm red-shift on UV−vis absorption spectra compared to the experimental value. The maximum wavelength at about 530 nm is the result of the HOMO to LUMO electron transition. SI Figure S5a shows that the HOMO of D149 is located on the main chain of molecule (indoline moiety), whereas the LUMO is mainly located on the rhodanine moiety.

DOI: 10.1021/am5068645
ACS Appl. Mater. Interfaces 2015, 7, 1568−1577

Table 1. Dye Absorption Coefficients and Solar Cell *I*−*V* Curve Characteristics under 100 mW.cm^{-2}, AM 1.5 G Filtered Illumination

dye	ε/mol^{-1}.L.cm^{-1} (λ_{max})[a]	nanostructure	d[b]/μm	V_{oc}/V	J_{sc}/mA.cm^{-2}	FF/%	η/% (mean value)	α	β
D149[c]	72 350 (530 nm)	NR35	19.4	0.548	12.68	69.3	4.82 (4.66 ± 4%)	0.103	0.613
		AG200	30.0	0.527	12.67	68.6	4.58 (4.36 ± 5%)	0.112	0.597
TG6[d]	22 450 (550 nm)	NR35	16.6	0.530	15.70	64.2	5.30 (5.06 ± 5%)	0.118	0.670
		AG200	22.0	0.532	12.28	71.5	4.67 (4.50 ± 4%)	0.136	0.717

[a]Absorption coefficient measured in DMF. For comparison ε_{N719} = 13 610 mol^{-1}.L.cm^{-1} (λ_{max} = 524 nm). [b]Film thickness. [c]D149 electrolyte composition: 0.05 mol·L^{-1} I_2 and 0.5 mol·L^{-1} 1,2-dimethyl-3-propylimidazolium iodide (DMPII) in acetonitrile. [d]TG6 electrolyte composition: 0.6 mol·L^{-1} 1,2-dimethyl-3-propylimidazolium iodide (DMPII), 0.1 mol·L^{-1} LiI, 0.05 mol·L^{-1} I_2, 0.10 mol·L^{-1} guanidinium thiocyanate, and 0.5 mol·L^{-1} 4-*tert*-butylpyridine in a mixture of acetonitrile and valeronitrile (85/15 volume ratio).

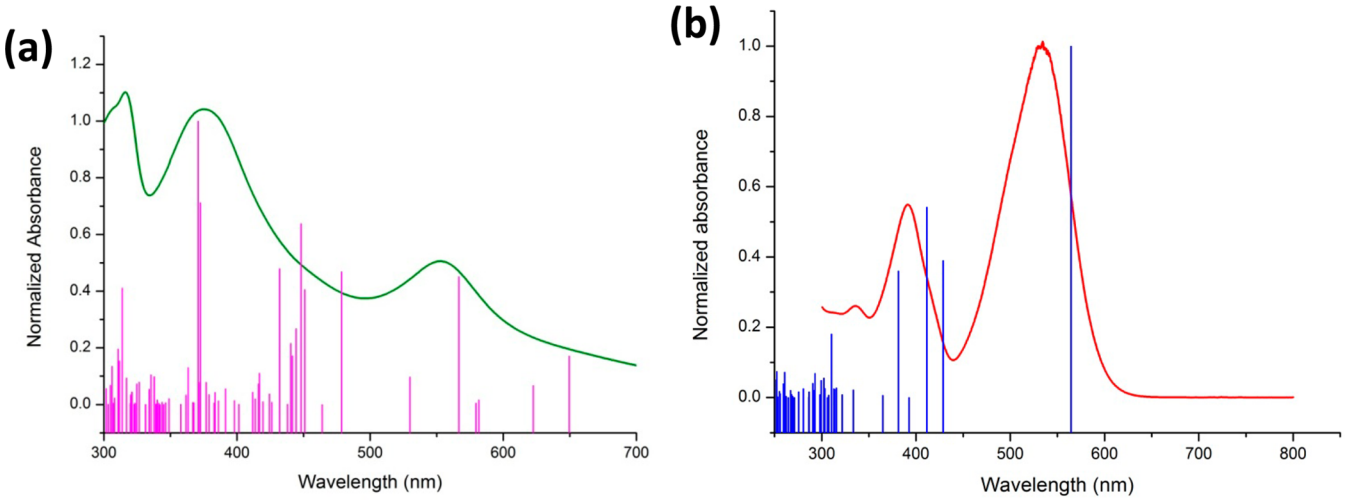

Figure 4. UV−vis spectra of (a) TG6 in CH_2Cl_2 (green: experimental; purple: computational) and (b) D149 in DMF (red: experimental; blue: computational).

The separation in the HOMO and LUMO positions indicates that the transition has an ICT (intramoleculer charge transfer) character.[54] This result is in line with the previous ones which compared the electronic structure of the D149 dye.[55,56]

The calculated molecular orbital energy levels for both dyes involved in main electronic transition together with the energy level of the conduction band (CB) and valence band (VB) of ZnO and also the energy position of I^-/I_3^- are presented in SI Figure S6. The energy levels of ZnO were extracted from ref 57 SI Figure S6 shows that the position of the LUMO energy of both dyes meets the criteria for an efficient charge injection to the ZnO conduction band. It requires the position of LUMO to be above the semiconductor conduction band. Similarly, for the dye regeneration, the position of the HOMO energy level must be below the electrolyte potential redox. These positions guarantee a sufficient driving force for electrons to flow.[55]

Our computational analysis outlines two important differences between the electronic properties of D149 and TG6 dyes. First, from the absorbance spectra, we can see that there are more electronic transitions in TG6 in the UV−vis range compared to that in D149, which makes the TG6 spectra broader compared to that of D149. Second, SI Figure S5c shows us that in TG6 the LUMO orbital is localized closer to the anchoring site carboxylate compared to that of D149, which indicates that the electron will transfer easily from the LUMO to the conduction band of ZnO.

The absorbance curves of the sensitized layers are presented in Figure 5A. For the sake of comparison they are reported per micrometer thickness unit. The maximum of the layer absorbance is higher for D149 compared to TG6 but in a much lower extent than the difference in their absorption coefficient. Therefore, we conclude with a higher TG6 dye concentration in the layers compared to D149. We also observe that the maxima of absorbance for the D149 and the TG6 dyes are higher for the AG200 films compared to the NR35 ones. In Figure 5B, the spectra have been normalized in order to show the effect of the aggregate on the optical properties. The absorbance of AG200-based layers is extended, especially in the red spectral region, due to multiple light scattering and then to prolonged light-traveling distance in these layers. The aggregates within ZnO films act as efficient scatterers for visible light, resulting in a significant increase in the light-harvesting capability of the photoelectrodes.

DSSCs have been prepared with the two different ZnO nanostructures and the organic metal-free and the Ru-polypyridyl complex dyes. Figure 6 shows typical *I*−*V* curves of the various investigated solar cells optimized for their performance. The cell PV parameters are gathered in Table 1. All the cells possessed a similar open circuit voltage of approximately 530−540 mV. This parameter was not significantly affected by the electrolyte composition (Table 1). However, the short circuit current density varied with the oxide structure and dye. The best performance was achieved for the NR35_TG6 cell and a power conversion efficiency of 5.30% was achieved with V_{oc} = 0.530 V, J_{sc} = 15.70 mA.cm^{-2}, and a fill factor, FF = 0.642. This represents a significant improvement compared to our previous record cells that were based on indoline dyes.[23,34,36] Hence, the use of TG6 dye in place of D149 dye significantly enhanced the cell J_{sc}. The incident photon-to-electron-conversion efficiency (IPCE)

DOI: 10.1021/am5068645
ACS Appl. Mater. Interfaces 2015, 7, 1568−1577

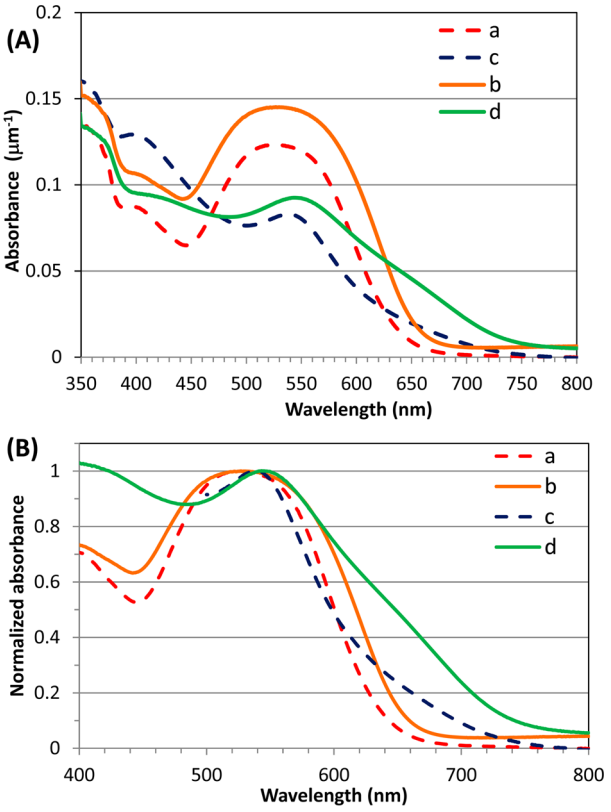

Figure 5. (A) Absorbance of the sensitized layers (reported by micrometer). (B) Absorbance normalized at the dye absorption maximum. (a) NR35_D149, (b) AG200_D149, (c) NR35_TG6, and (d) AG200_TG6.

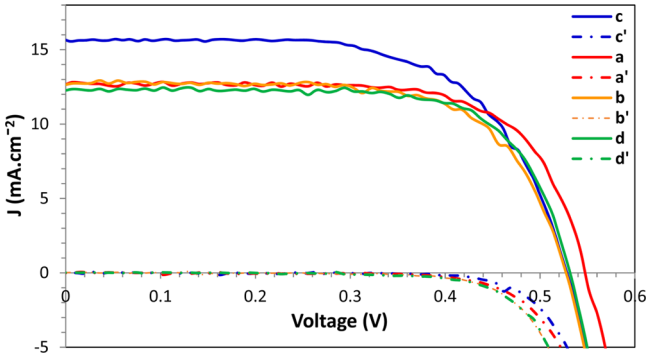

Figure 6. *I*–*V* curves under 1 sun illumination of the investigated solar cells. (a) NR35_D149, (b) AG200_D149, (c) NR35_TG6, and (d) AG200_TG6. The dashed lines are the dark currents of the cells (a′-d′).

curves presented in SI Figure S7 show that the TG6 cell has a broader action spectrum and that the larger J_{sc} is the result of an improved sunlight collection.

In Table 1, the performances of the AG200-based solar cells were lower than those of the NR35-based ones in spite of a higher dye concentration. This suggests the presence of dye agglomerates in that case. The performances of DSSCs depend on the two types of processes experienced by the electrons injected to the oxide conduction band from the excited dye: the transport and the recombination reaction. The transport is a forward movement of electrons to a back contact collector as a result of a gradient of electron concentration. It is a field-free random walk process. In the generally accepted multiple trapping (MT) model,[58−60] the electrons are considered to be mostly trapped in localized states below the conduction band edge, from which they can escape by thermal activation. The electron movement is characterized by the transport time (τ_{tr}), which is the mean time for the electron to reach the back contact. Recombination is a back flow of electrons to tri-iodide ions (and oxidized dyes) characterized by the electron lifetime (τ_n).

Impedance spectroscopy (IS) is a powerful technique that has been employed in a large extent to investigate the coupled kinetics of electrochemical and photoelectrochemical reactions occurring in DSSCs.[6,58−64] DSSCs of similar thickness (between 16 and 17 μm) have been prepared and investigated by IS. Examples of spectra are presented in SI Figure S8. They have been analyzed according to the multiple trapping (MT) model.[65] They all showed a characteristic low-middle frequency semicircle due to the resistance to charge transfer (recombination) (R_{ct}) across the sensitized oxide-electrolyte interface coupled to the total electrode capacitance, denoted as C_μ, which is a chemical capacitance due to filled trap states localized below the conduction band minimum. At high frequency, a second semicircle was found due to the resistance (R_{Pt}) and capacitance (C_{Pt}) of the charged counter electrode/electrolyte interface. In the intermediate frequency range, a ∼45° straight-line segment could be clearly observed for cells polarized at not too high applied voltage, which is characteristic of the electron transport by diffusion and is modeled by a transport resistance, noted as R_{tr} in Figure 7A. The high frequency series resistance, R_s, is due to the electrical contacts. The full equivalent circuit used to fit the spectra is presented in Figure 7A. We noted that for all the investigated cells the IS spectra did not exhibit a clear Warburg loop at low frequency, even at a high applied voltage (not shown). This clearly excludes a performance limitation due to the diffusion of the I^-/I_3^- redox shuttle.

C_μ is a chemical capacitance due to filled trap states localized below the conduction band minimum (sub-band gap state). C_μ is plotted as a function of V_{cor} in Figure 7B and it varies more or less exponentially as expected for the model used. The experimental data have been fitted by the relationship:[6]

$$C_\mu = C_{0,\mu} \exp\left[\alpha \frac{qV_{cor}}{k_B T}\right] = C_{0,\mu} \exp\left[\frac{qV_{cor}}{k_B T_0}\right] \quad (1)$$

where k_B is the Boltzmann constant (1.381×10^{-23} $m^2.kg.s^{-2}.K^{-1}$), T the absolute temperature, and q the elementary charge (1.602×10^{-19} C). The C_μ curves of AG200 based solar cells are negatively shifted compared to the NR35 ones which suggests a negative energy shift of the conduction band minimum (CBM) of ZnO in the case of the aggregates. α is a parameter that accounts for the depth of the trap energy distribution below the conduction band. In Figure 7B, α value ranges between 0.10 and 0.14 (Table 1) and are slightly lower than those of anatase and brookite TiO_2 that we have measured recently as ranging 0.18−0.23.[66]

In Figure 7C, R_{ct} is presented versus V_{cor}. Slightly less recombinations are found for the TG6-sensitized solar cells that can be assigned to the presence of the two long alkyl chains in the molecular structure of the dye and to its amphiphilic character. R_{ct} show an exponential variation, in agreement with the MT model, that follows the relationship[6]

$$R_{ct} = R_{0,ct} \exp\left[-\beta \frac{qV_{cor}}{k_B T}\right] \quad (2)$$

DOI: 10.1021/am5068645
ACS Appl. Mater. Interfaces 2015, 7, 1568−1577

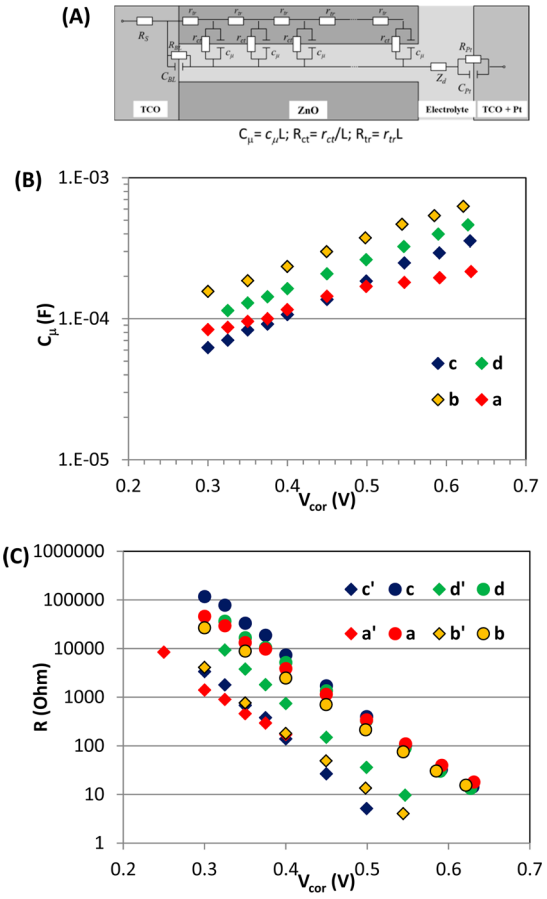

Figure 7. (A) Equivalent electrical circuit used to fit the impedance spectra. (B) Variation of C_μ with V_{cor}. (C) Variation of R_{ct} (a, b, c, d) and R_{tr} (a′, b′, c′, d′) with V_{cor}.(a, a′) NR35_D149, (b, b′) AG200_D149, (c, c′) NR35_TG6, and (d, d′) AG200_TG6.

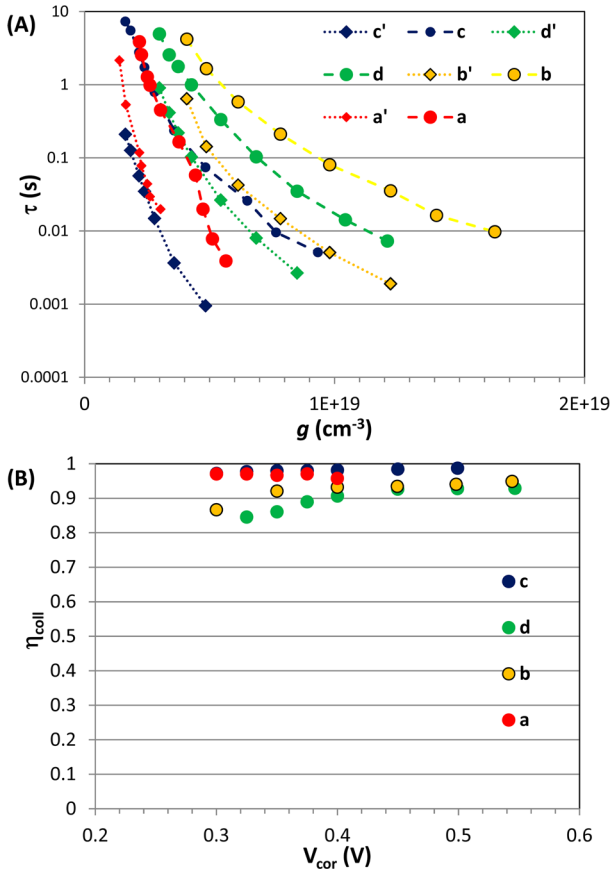

Figure 8. (A) τ_n and τ_{tr} versus g. (B) η_{coll} versus g (a) NR35_D149, (b) AG200_D149, (c) NR35_TG6, and (d) AG200_TG6.

where β can be considered an estimation of the reaction order. β values range between 0.60 and 0.72 depending on the dye and on the structure (Table 1). β of TG6-sensitized DSSC is significantly higher than β of D149-sensitized ones. β lower than 1 is an empirical way to describe sublinear recombination kinetics that takes into account that electrons may be transferred from occupied levels located in the energy gap.[67−69]

The electron lifetime, τ_n, is the mean time before the charge recombination with the tri-iodide species in solution. It has been calculated according to $\tau_n = R_{ct}C_\mu$.[64] Due to the different trap state distribution and conduction band level for the various photoelectrodes, this parameter has been compared as a function of the trapped electron concentration, g. From C_μ, g was calculated according to[6]

$$g(V_{cor}) = \frac{C_\mu(V_{cor})}{qAd(1-p)} \tag{3}$$

where A is the geometric area of the cell, d the oxide layer thickness, and p the film porosity. τ_n is displayed in Figure 8A. It decreases with the applied potential (and then g) because the electron interception increases with the driving force. τ_n is significantly longer for the aggregate-based cells compared to the nanorod ones. We can suppose that it is due to the charge confinement in these rather large objects. The transport time is the mean time for the photogenerated electrons to reach the back contact. It was calculated as $\tau_{tr} = R_{tr}C_\mu$.[64] The R_{tr} parameter describes the transport properties of the films and is presented in Figure 7C. For all the cells it varies exponentially and is significantly lower than R_{ct}. τ_{tr} is plotted as a function of g in Figure 8A. Longer transport times are found for the aggregates. It shows that this structure is detrimental for the electron traveling. However, for all the cells τ_n is more than 1 order of magnitude higher than τ_{tr}, a difference that ensures a rather good charge collection at the FTO contact. The charge collection efficiency, η_{coll}, in the photoelectrodes was calculated using the following classical relationship:[3]

$$\eta_{coll} = \frac{1}{\left(1 + \frac{\tau_{tr}}{\tau_n}\right)} \tag{4}$$

The results are displayed in Figure 8B. The collection efficiency is very high in the case of NR35-based cells with values higher than 96%. On the other hand, significantly lower values (86−95%) are found in the case of AG200 solar cells. Therefore, cell performance losses are expected for the AG200-based DSSCs.

The conductivity of ZnO porous layers was determined from the charge transport resistance:[6]

$$\sigma_n = \frac{d}{A(1-p)R_{tr}} \tag{5}$$

Figure 9A shows the conductivity of NR35 and AG200 layers as a function of g. σ_n increases rapidly with this parameter due to the trap filling. We observe that the conductivity is not significantly changed with the sensitizer. On the other hand, it depends on the ZnO nanostructure. The conductivity of the

DOI: 10.1021/am5068645
ACS Appl. Mater. Interfaces 2015, 7, 1568−1577

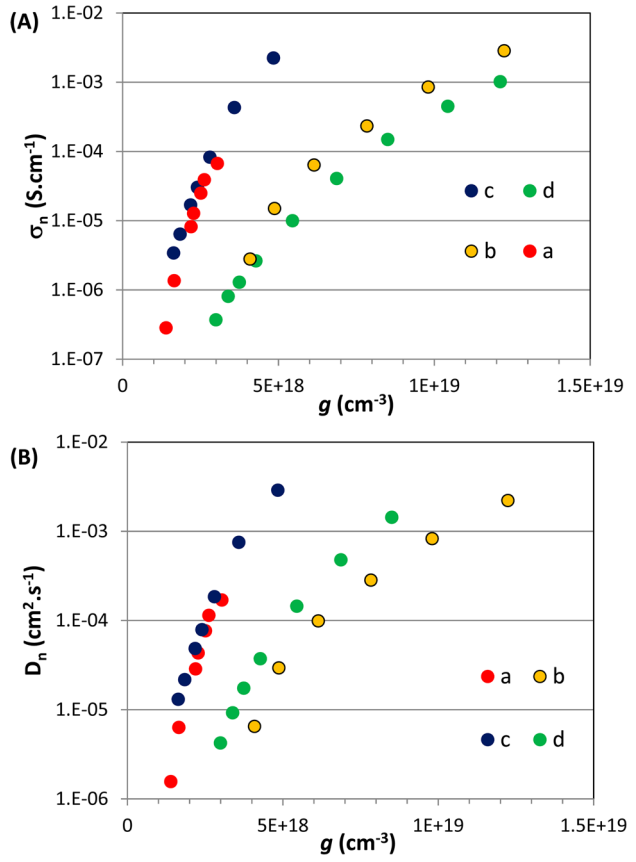

Figure 9. (A) σ_n versus g. (B) D_n versus g. (a) NR35_D149, (b) AG200_D149, (c) NR35_TG6, and (d) AG200_TG6.

NR35 layers is much higher than the AG200 one. This shows that the electrical connection between the submicrometer-sized spheres is significantly poorer than that between the nanorods. These spheres are more difficult to sinter than the nanorods. From τ_n and τ_{tr} measured by IS, we have also estimated the effect of the ZnO structure on the chemical diffusion coefficient of electrons, denoted as D_n.

$$D_n = d^2/\tau_{tr} \tag{6}$$

In Figure 9B, D_n is plotted as a function of g. As expected, the behavior is similar to that found for σ_n and D_n is much larger for NR35 layers compared to the AG200 ones.

Using the IS data, we have also determined the electron diffusion length (L_n) defined as the average distance traveled by the electrons in ZnO before recombination. This parameter is given by[6]

$$L_n = \sqrt{D_n\tau_n} = d\sqrt{\frac{\tau_n}{\tau_{tr}}} \tag{7}$$

The results are displayed in Figure 10. Two different behaviors are observed: L_n is longer than 100 nm in the case of the NR35 layers and significantly shorter in the case of AG200 photoelectrodes.

CONCLUSIONS

In conclusion, we have introduced the use of a ruthenium polypyridyl dye containing a hexasulfanyl-styryl modified bipyridyl group as ancillary ligand, coded TG6, for ZnO photoelectrode sensitization. This dye has been investigated for

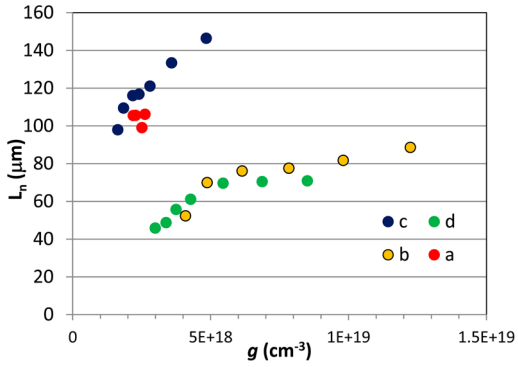

Figure 10. L_n versus g. (a) NR35_D149, (b) AG200_D149, (c) NR35_TG6, and (d) AG200_TG6.

the sensitization of porous layers made of sintered nanorod particles and nanocrystallite spherical aggregates and it has been compared to the metal-free D149 organic dye. The AG200 layers show a remarkable reflectance in the visible wavelength region, but poor crystallographic quality. They adsorb more dye than the NR35 layers but do not generate more current when they are used as building blocks of photoelectrodes. TG6 attached to ZnO has a broaden absorbance spectrum in the blue and red regions compared to the D149 dye and then ensures a better sunlight harvesting. We have shown that TG6 is highly relevant combined with porous NR35 photoelectrodes made of ZnO rod-like nanoparticles and the optimal power conversion efficiency has been measured at 5.30%. The impedance spectroscopy study carried out over a large applied voltage range has shown that at high applied voltage R_{ct} is similar for the various investigated solar cell and explains the similar V_{oc}. The electron lifetime is longer in the aggregates but the transport time is also longer. On the whole, the charge collection is more efficient in the NR35 photoelectrodes. The conductivity measurements show that the NR35 layers are more conducting than the AG200 ones. The electrical connections that result from the sintering process are much better for the nanorods compared to the spheres.

ASSOCIATED CONTENT

Supporting Information

Effect of AG200 layer annealing temperature on the cell parameters, effect of aggregate layer thickness on the cell parameters, particle and aggregate size distribution diagrams, XRD patterns of NR35 and AG200 ZnO films and particle size calculations, calculated TD-DFT spectra of TG6 and D149, HOMO and LUMO orbitals of D149 and TG6 dyes, energy diagram of the investigated systems, and typical EIS spectra. This material is available free of charge via the Internet at http://pubs.acs.org.

AUTHOR INFORMATION

Corresponding Author

*E-mail: thierry.pauporte@chimie-paristech.fr. Tel.: (33)1 55 42 63 83.

Notes

The authors declare no competing financial interest.

ACKNOWLEDGMENTS

Borun chemicals is acknowledged for providing us with the TG6 dye. The authors acknowledge the French SEAM labex for

DOI: 10.1021/am5068645
ACS Appl. Mater. Interfaces 2015, 7, 1568−1577

financial support (PR-F-2012 project). Yuly Kusumawati acknowledges Campus France and the Higher Education Ministry of Indonesia (DIKTI) government for financial support in the framework of the DDIP collaboration program. Dr. Bruno Viana and Patrick Aschehoug (IRCP_Paris, France) are thanked for PL spectrum measurements.

REFERENCES

(1) O'Regan, B.; M. Grätzel, M. A Low-Cost High-Efficiency Solar Cell Based on Dye-Sensitized Colloidal TiO_2 Films. *Nature* **1991**, *353*, 737−740.
(2) Kalyanasundaram, K. *Dye-Sensitized Solar Cells*; EPFL press: Lausanne, 2010.
(3) Hagfeldt, A.; Boschloo, G.; Sun, L.; Kloo, L.; Pettersson, H. Dye-Sensitized Solar Cells. *Chem. Rev.* **2010**, *110*, 6595−6663.
(4) Yella, A.; Lee, H.-W.; Tsao, H. N.; Yi, C.; Chandiran, A. K.; Nazeeruddin, M. K.; Wei-Guang Diau, E.; Yeh, C.-Y.; Zakeeruddin, S. M.; Grätzel, M. Porphyrin-Sensitized Solar Cells with Cobalt (II/III)-Based Redox Electrolyte Exceed 12% Efficiency. *Science* **2011**, *334*, 629−634.
(5) Law, M.; Greene, L. E.; Johnson, J. C.; Saykally, R.; Yang, P. Nanowire Dye-Sensitized Solar Cells. *Nat. Mater.* **2005**, *4*, 455−459.
(6) Magne, C.; Moehl, T.; Urien, M.; Grätzel, M.; Pauporté, T. Effects of ZnO Film Growth Route and Nanostructure on Electron Transport and Recombination in Dye-Sensitized Solar Cells. *J. Mater. Chem. A* **2013**, *1*, 2079−2088.
(7) Martinson, A. B.; Goes, M. S.; Fabregat-Santiago, F.; Bisquert, J.; Pellin, M. J.; Hupp, J. T. Electron Transport in Dye-Sensitized Solar Cells Based on ZnO Nanotubes: Evidence for Highly Efficient Charge Collection and Exceptionally Rapid Dynamics. *J. Phys. Chem. A* **2009**, *113*, 4015.
(8) Le Bahers, T.; Labat, F.; Pauporté, T.; Ciofini, I. Solvent and Additives Effects on the Open Circuit Voltage of ZnO Based Dye-Sensitized Solar Cells: A Combined Theoretical and Experimental Study. *Phys. Chem. Chem. Phys.* **2010**, *12*, 14710−14719.
(9) Zhang, Q.; Chou, T. P.; Russo, B.; Jenekhe, S. A.; Cao, G. Aggregation of ZnO Nanocrystallites for High Conversion Efficiency in Dye-Sensitized Solar Cells. *Angew. Chem., Int. Ed.* **2008**, *47*, 2402−2406.
(10) Cheng, H.; Hsieh, W. High Efficiency Metal-Free Organic-Dye-Sensitized Solar Cells with Hierarchical ZnO Photoelectrode. *Energy Environ. Sci.* **2010**, *3*, 442−447.
(11) Cheng, H.; Hsieh, W. Electron Transfer Properties of Organic Dye-Sensitized Solar Cells Based on Indoline-Sensitizers with ZnO Nanoparticles. *Nanotechnology* **2010**, *21*, 485202.
(12) Lupan, O.; Guérin, V. M.; Tiginyanu, I. M.; Ursaki, V. V.; Chow, L.; Heinrich, H.; Pauporté, T. Vertically-Oriented Well-Aligned ZnO Nanowires Arrays Electrodeposited on ITO- Coated Glass and Their Integration in Dye-Sensitized Solar Cells. *J. Photochem. Photobiol., A* **2010**, *211*, 65−73.
(13) Elbelghiti, H.; Pauporté, T.; Lincot, D. Mechanistic Study of ZnO Nanorod Array Electrodeposition. *Phys. Status Solidi A* **2008**, *205*, 2360−2364.
(14) Guérin, V. M.; Pauporté, T. From Nanowires to Hierarchical Structures of Template-Free Electrodeposited ZnO for Efficient Dye-Sensitized Solar Cells. *Energy Environ. Sci.* **2011**, *4*, 2971−2979.
(15) Guérin, V. M.; Elias, J.; Nguyen, T. T.; Philippe, L.; Pauporté, T. Ordered Networks of ZnO-Nanowire Hierarchical Urchin-Like Structures for Improved Dye-Sensitized Solar Cells. *Phys. Chem. Chem. Phys.* **2012**, *14*, 12948−12955.
(16) Lee, S.; Jeong, S.; Kim, D.; Hwang, S.; Jeon, M.; Moon, J. ZnO Nanoparticles with Controlled Shapes and Sizes Prepared Using a Simple Polyol Synthesis. *Superlattice Microstruct.* **2008**, *43*, 330−339.
(17) Poul, L.; Jouini, N.; Fiévet, F. Layered Hydroxide Metal Acetates (Metal = Zinc, Cobalt and Nickel): Elaboration via Hydrolysis in Polyol Medium and Comparative Study. *Chem. Mater.* **2000**, *12*, 3123−3132.
(18) Couto, G. G.; Klein, J. J.; Schreiner, W. H.; Mosca, D. H.; De Oliveira, A. J. A.; Zarbin, A. J. G. Nickel Nanoparticles Obtained by a Modified Polyol Process: Synthesis, Characterization, and Magnetic Properties. *J. Colloid Interface Sci.* **2007**, *311*, 461−468.
(19) Kodama, D.; Shinoda, K.; Sato, K.; Sato, Y.; Jeyadevan, B.; Tohji, K. Synthesis of Size-Controlled Fe−Co Alloy Nanoparticles by Modified Polyol Process. *J. Magn. Magn. Mater.* **2007**, *310*, 2396−2398.
(20) Collins, I. R.; Taylor, S. E. Non-Aqueous Thermal-Decomposition Route to Colloidal Inorganic Oxides. *J. Mater. Chem.* **1992**, *2*, 1277−1281.
(21) Dakhlaoui, A.; Jendoubi, M.; Smiri, L. S.; Kanaev, A.; Jouini, N. Synthesis, Chraracterization and Optical Properties of ZnO Nanoparticles with Controlled Size and Morphology. *J. Crystal Growth* **2009**, *311*, 3989−3996.
(22) Bell, N. S.; Tallant, D. R. Ripening and Growth of Zinc Oxide Nanorods From Nanoparticles in 1,4 Butanediol Solvent. *J. Sol-Gel Sci. Technol.* **2009**, *51*, 158−168.
(23) Hosni, M.; Kusumawati, Y.; Farhat, S.; Jouini, N.; Pauporté, T. Effects of Oxide Nanoparticle Size and Shape on Electronic Structure, Charge Transport and Recombination in Dye-Sensitized Solar Cell Photoelectrodes. *J. Phys. Chem. C* **2014**, *118*, 16791−16798.
(24) Trenque, I.; Mornet, S.; Duguet, E.; Gaudon, M. New Insights into Crystallite Size and Cell Parameters Correlation for ZnO Nanoparticles Obtained from Polyol-Mediated Synthesis. *Inorg. Chem.* **2013**, *52*, 12811−12817.
(25) Ren, Y.; Zhen, Y. Z.; Zhao, J.; Chen, J. F.; Zhou, W.; Tao, X. A Comparative Study on Indoline Dye- and Ruthenium Complex-Sensitized Hierarchically Structured ZnO Solar Cells. *Electrochem. Commun.* **2012**, *16*, 57−60.
(26) Pauporté, T.; Magne, C. Impedance Spectroscopy Study of N719-Sensitized ZnO-Based Solar Cells. *Thin Solid Films* **2014**, *560*, 20−26.
(27) Saito, M.; Fujihara, S. Large Photocurrent Generation in Dye-Sensitized ZnO Solar Cells. *Energy Environ. Sci.* **2008**, *1*, 280−283.
(28) Memarian, N.; Concina, I.; Braga, A.; Rozati, S. M.; Vomiero, A.; Sberveglieri, G. Hierarchically Assembled ZnO Nanocrystallites for High-Efficiency Dye-Sensitized Solar Cells. *Angew. Chem.* **2011**, *123*, 12529−12533.
(29) Chen, L. Y.; Yin, Y. T. Efficient Electron Transport in ZnO Nanowire/Nanoparticle Dye-Sensitized Solar Cells via Continuous Flow Injection Process. *RSC Adv.* **2013**, *3*, 8480−8488.
(30) Keis, K.; Lindgren, J.; Lindquist, S. E.; Hagfeldt, A. Studies of the Adsorption Process of Ru Complexes in Nanoporous ZnO Electrodes. *Langmuir* **2000**, *16*, 4688−4694.
(31) Bedja, I.; Kamat, P. V.; Hua, X.; Lappin, P. G.; Hotchandani, S. Photosensitization of Nanocrystalline ZnO Films by Bis(2,2′-bipyridine)(2,2′-bipyridine-4,4′-dicarboxylic acid)ruthenium(II). *Langmuir* **1997**, *13*, 2398−2403.
(32) Horiuchi, H.; Kaoh, R.; Hara, K.; Yanagida, M.; Murata, S.; Arakawa, H.; Tachiya, M. Electron Injection Efficiency from Excited N3 into Nanocrystalline ZnO Films: Effect of(N3-Zn^{2+}) Aggregate Formation. *J. Phys. Chem. B* **2003**, *107*, 2570−2574.
(33) Howie, W. H.; Claeyssens, F.; Miura, H.; Peter, L. M. Characterization of Solid-State Dye-Sensitized Solar Cells Utilizing High Absorption Coefficient Metal-Free Organic Dyes. *J. Am. Chem. Soc.* **2008**, *130*, 1367−1375.
(34) Guérin, V. M.; Magne, C.; Pauporté, T.; Le Bahers, T.; Rathousky, J. Nanoporous Electrodeposited versus Nanoparticulate ZnO Porous Films of Similar Roughness for Dye Sensitized Solar Cell Application. *ACS Appl. Mater. Interfaces* **2010**, *2*, 3677−3685.
(35) Yoshida, T.; Zhang, J.; Komatsu, D.; Sawatani, S.; Minoura, H.; Pauporté, T.; Lincot, D.; Oekermann, T.; Schlettwein, D.; Tada, H.; Wörhle, D.; Funabiki, K.; Matsui, M.; Miura, H.; Yanagi, H. Electrodeposition of Inorganic/Organic Hybrid Thin Films. *Adv. Funct. Mater.* **2009**, *19*, 17−43.
(36) Magne, C.; Urien, M.; Pauporté, T. Enhancement of Photovoltaic Performances in Dye-Sensitized Solar Cells by Co-

DOI: 10.1021/am5068645
ACS Appl. Mater. Interfaces 2015, 7, 1568−1577

Sensitization with Metal-Free Organic Dyes. *RSC Adv.* **2013**, *3*, 6315−6318.
(37) Higashijima, S.; Miura, H.; Fujita, T.; Kubota, Y.; Funabiki, K.; Yoshida, T.; Matsui, M. Highly Efficient New Indoline Dye Having Strong Electron-Withdrawing Group for Zinc Oxide Dye-Sensitized Solar Cell. *Tetrahedron* **2011**, *167*, 6289−6293.
(38) Higashijima, S.; Inoue, Y.; Miura, H.; Kubota, Y.; Funabiki, K.; Yoshida, T.; Matsui, M. Organic Dyes Containing Fluorene-Substituted Indoline Core for Zinc Oxide Dye-Sensitized Solar Cell. *RSC Adv.* **2012**, *2*, 2721−2724.
(39) Matar, F.; Ghaddar, T. H.; Walley, K.; DosSantos, T.; Durrant, J. R.; O'Regan, B. A New Ruthenium Polypyridyl Dye, TG6, whose Performance in Dye-Sensitized Solar Cells is Surprisingly Close to that of N719, the Dye to Beat for 17 Years. *J. Mater. Chem.* **2008**, *18*, 4246−4253.
(40) O'Regan, B.; Li Xiaoe, L.; Ghaddar, T. Dye Adsorption, Desorption, and Distribution in Mesoporous TiO_2 Films, and Its Effects on Recombination Losses in Dye-Sensitized Solar Cells. *Energy Environ. Sci.* **2012**, *5*, 7203−7215.
(41) Frisch, M. J.; Trucks, G. W.; Schlegel, H. B.; Scuseria, G. E.; Robb, M. A.; Cheeseman, J. R.; Scalmani, G.; Barone, V.; Mennucci, B.; Petersson, G. A.; Nakatsuji, H.; Caricato, M.; Li, X.; Hratchian, H. P.; Izmaylov, A. F.; Bloino, J.; Zheng, G.; Sonnenberg, J. L.; Hada, M.; Ehara, M.; Toyota, K.; Fukuda, R.; Hasegawa, J.; Ishida, M.; Nakajima, T.; Honda, Y.; Kitao, O.; Nakai, H.; Vreven, T.; Montgomery, J. A., Jr.; Peralta, J. E.; Ogliaro, F.; Bearpark, M.; Heyd, J. J.; Brothers, E.; Kudin, K. N.; Staroverov, V. N.; Kobayashi, R.; Normand, J.; Raghavachari, K.; Rendell, A.; Burant, J. C.; Iyengar, S. S.; Tomasi, J.; Cossi, M.; Rega, N.; Millam, M. J.; Klene, M.; Knox, J. E.; Cross, J. B.; Bakken, V.; Adamo, C.; Jaramillo, J.; Gomperts, R.; Stratmann, R. E.; Yazyev, O.; Austin, A. J.; Cammi, R.; Pomelli, C.; Ochterski, J. W.; Martin, R. L.; Morokuma, K.; Zakrzewski, V. G.; Voth, G. A.; Salvador, P.; Dannenberg, J. J.; Dapprich, S.; Daniels, A. D.; Farkas, Ö.; Foresman, J. B.; Ortiz, J. V.; Cioslowski, J.; Fox, D. J. *Gaussian 09*, Revision A.1; Gaussian, Inc.: Wallingford, CT, 2009.
(42) Becke, A. D. Density-Functional Thermochemistry. III. The Role of Exact Exchange. *J. Chem. Phys.* **1993**, *98*, 5648−5652.
(43) McLean, A. D.; Chandler, G. S. Contracted Gaussian Basis Set for Molecular Calculations. I. Second Row Atom, Z=11−18. *J. Chem. Phys.* **1980**, *72*, 5639−5648.
(44) Krishnan, R.; Binkley, J. S.; Seeger, R.; Pople, J. A. Self-Consistent Molecular Orbital Methods. XX. A Basis Set for Correlated Wave Function. *J. Chem. Phys.* **1980**, *72*, 650−654.
(45) Dunning, T. H., Jr.; Hay, P. J. In *Modern Theoretical Chemistry*; Schaefer, H. F., Ed.; Plenum: New York, 1977; Vol. 3, pp 1−28.
(46) Hay, P. J.; Wadt, W. R. Initio Effective Core Potentials for Molecular Calculations. Potentials for Transition Metal Atom Sc to Hg. *J. Chem. Phys.* **1985**, *82*, 270−283.
(47) Wadt, W. R.; Hay, P. J. Ab Initio Effective Core Potentials for Molecular Calculations. Potentials for K to Au Including Outermost Core Orbitals. *J. Chem. Phys.* **1985**, *82*, 299−310.
(48) Cossi, M.; Barone, V. Polarizable Dielectric Model of Solvation with Inclusion of Charge Penetration Effects. *J. Chem. Phys.* **2001**, *115*, 4708−4717.
(49) Cossi, M.; Rega, N.; Scalmani, G.; Barone, V. Energies, Structures, and Electronic Properties of Molecules in Solution with C-PCM Solvation Model. *J. Comput. Chem.* **2003**, *24*, 669−681.
(50) Runge, E.; Gross, E. K. U. Density-Functional Theory for Time-Dependent Systems. *Phys. Rev. Lett.* **1984**, *52*, 997−1000.
(51) Van de Hulst, H. C. *Light Scattering by Small Particles*; Wiley: New York, 1957.
(52) Wolf, P. E.; Maret, G. Weak Localization and Coherent Backscattering of Photons in Disordered Media. *Phys. Rev. Lett.* **1985**, *55*, 2696−2699.
(53) Magne, C.; Urien, M.; Pauporté, T. Growth of Porous Light Scattering Sub-micrometer particle films by Occlusion Electrolysis for Dye-Sensitized Solar Cells. *Electrochim. Acta* **2013**, *110*, 382−386.
(54) Ham, H. W.; Kim, Y. S. Theoretical Study of Indoline Dyes for Dye-Sensitized Solar Cells. *Thin Solid Films* **2010**, *518*, 6558−6563.
(55) Le Bahers, T.; Pauporté, T.; Scalmani, G.; Adamo, C.; Ciofini, I. *A TD-DFT* Investigation of Ground and Excited State Properties in Indoline Dyes used for Dye-Sensitized solar cells. *Phys. Chem. Chem. Phys.* **2009**, *11*, 11276−11284.
(56) Kim, J. Y.; Kim, Y. H.; Kim, Y. S. Indoline Dyes with Various Acceptors for Dye-Sensitized Solar Cells. *Curr. Appl. Phys.* **2011**, *11*, S117−S121.
(57) Lee, T. H.; Sue, H. J.; Cheng, X. Solid-state Dye-Sensitized Solar Cells Based on ZnO Nanoparticle and Nanorod Array Hybrid Photoanodes. *Nanoscale Res.* **2011**, *6*, 517.
(58) Bisquert, J.; Vikhrenko, V. S. Interpretation of the Time Constants Measured by Kinetic Techniques in Nanostructured Semiconductor Electrodes and Dye-Sensitized Solar Cells. *J. Phys. Chem. B* **2004**, *108*, 2313−2322.
(59) Fisher, A. C.; Peter, L. M.; Ponomarev, E. A.; Walker, A. B.; Wijayantha, K. G. U. Intensity Dependence of the Back Reaction and Transport of Electrons in Dye-Sensitized Nanocrystalline TiO_2 Solar Cells. *J. Phys. Chem. B* **2000**, *104*, 949−958.
(60) Bisquert, J. Theory of the Impedance of Electron Diffusion and Recombination in a Thin Layer. *J. Phys. Chem. B* **2002**, *106*, 325−333.
(61) Bisquert, J. Chemical Diffusion Coefficient of Electrons in Nanostructured Semiconductor Electrodes and Dye-Sensitized Solar Cells. *J. Phys. Chem. B* **2004**, *108*, 2323−2332.
(62) Hauch, A.; Georg, A. Diffusion in the Electrolyte and Charge-Transfer Reaction at the Platinum Electrode in Dye-Sensitized Solar Cells. *Electrochim. Acta* **2001**, *46*, 3457−3466.
(63) Adachi, M.; Sakamoto, M.; Jiu, J.; Ogata, Y.; Isoda, S. Determination of Parameters of Electron Transport in Dye-Sensitized Solar Cells using Electrochemical Impedance Spectroscopy. *J. Phys. Chem. B* **2006**, *110*, 13872−13880.
(64) Fabregat-Santiago, F.; Bisquert, J.; Palomares, E.; Otero, E.; Kuang, D.; Zakeeruddin, S. M.; M. Grätzel, M. Correlation Between Photovoltaic Performance and Impedance Spectroscopy of Dye-Sensitized Solar Cells Based on Ionic Liquids. *J. Phys. Chem. C* **2007**, *111*, 6550−6560.
(65) Bisquert, J.; Fabregat-Santiago, F. In *Dye-Sensitized Solar Cells*; Kalyanasundaram, K., Ed.; EPFL Press: Lausanne, Switzerland, 2010; Chapter 12, pp 457−554.
(66) Kusumawati, Y.; Hosni, M.; Martoprawiro, M. A.; Cassaignon, S.; Pauporté, T. Charge Transport and Recombination in TiO_2 Brookite Photoelectrode. *J. Phys. Chem. C* **2014**, *118*, 23459−23467.
(67) Bisquert, J.; Mora-Sero, I. Simulation of Steady-State Characteristics of Dye-Sensitized Solar Cells and the Interpretation of the Diffusion Length. *J. Phys. Chem. Lett.* **2010**, *1*, 450−456.
(68) Villanueva-Cab, J.; Wang, H.; Oskam, G.; Peter, L. M. Electron Diffusion and Back Reaction in Dye-Sensitized Solar Cells: The Effect of Nonlinear Recombination Kinetics. *J. Phys. Chem. Lett.* **2010**, *1*, 748−751.
(69) Gonzalez-Vazquez, J. P.; Oskam, G.; Anta, J. A. Origin of Nonlinear Recombination in Dye-Sensitized Solar Cells: Interplay Between Charge Transport and Charge Transfer. *J. Phys. Chem. C* **2012**, *116*, 22687−22697.

DOI: 10.1021/am5068645
ACS Appl. Mater. Interfaces 2015, 7, 1568−1577